Phase change-based "switch-off" enabled toroidal dipole excitation in polarization - independent achiral metasurface in mid-infrared regime

SHIRISH TRIPATHI*, RITESH KUMAR MISHRA
Department of Electronics and Communication Engineering, National Institute of Technology, Patna, India

This study presents polarization-independent, achiral metasurface using $Ge_2Sb_2Te_5$ (GST)-integrated square spiral design on SiO_2-Au substrate for active modulation of toroidal dipole resonances in mid-infrared regime. FDTD simulations show strong field confinement with dominant toroidal dipoles in amorphous GST (AGST), while crystalline (CGST) suppresses resonances, enabling dynamic switching. Geometrical parameters, branch width, turn spacing and inter-segment gaps, govern spectral tuning and resonance sharpness. Multipolar decomposition confirms toroidal dominance under optimized dimensions. Results establish pathway for tunable, reconfigurable metasurface devices for high-Q sensing, mid-infrared modulation, biosensing, and environmental monitoring, supporting GST-based phase-switchable components in compact, efficient, responsive optoelectronic platforms.

(Received December 2, 2025; accepted June 2, 2026)

Keywords: Metasurface, Toroidal resonance, Phase-Change Material, $Ge_2Sb_2Te_5$

1. Introduction

Metasurfaces are subwavelength-engineered structures capable of controlling the light-matter interactions by modifying electromagnetic responses [1]. The attributes are highly contingent upon the design or architect, the materials employed, and the interfaces created by the layers and their dimensions; thus, response can be regulated by these factors [2, 3]. Recent years have witnessed a surge in extensive research for many applications, particularly in the field of non-contact/label-free optical sensors [4, 5]. Due to their ability to detect things quickly and reliably, optical sensing techniques are clearly very helpful in high-speed communication [6, 7], defense [8, 9], and contemporary biomedical and environmental monitoring [10, 11]. The mid-infrared (MIR) spectral region, in the 2-20 μm wavelength range, has gained importance due to their broad range of applications [12]. Promising quantum and nonlinear reactions and properties have been observed in many structures and designs. Furthermore, it has been shown that plasmonic meta-devices in the infrared range are considerably superior to traditional absorption-based spectroscopic approaches in demonstrating a variety of real-time biomolecule interactions and sensing [13].

The study of optical resonances in meta-devices is fundamentally based on the scattering phenomena of sub-wavelength resonators. Optical resonance can be induced by an oscillating displacement current, which consists of charged particles, when the effective wavelength of the incident light approximates the feature size of the entire design or a specific section of it. In metasurfaces, electromagnetic waves interact with the material to produce electric dipoles from oscillating charges and magnetic dipoles from circulating currents. The toroidal dipole, a distinctive phenomenon, occurs when magnetic dipoles are configured in particular arrangements, such as a complete loop in three dimensions or anti-parallel dipoles in two-dimensional planar metamaterials [14]. Due to interference between narrow and broad resonances, this configuration also produces acute, asymmetric Fano resonances [15]. By reducing net magnetic and electric dipole moments, the toroidal dipole arrangement improves electromagnetic (EM) energy confinement, sharpens resonant responses, and strengthens coupling with the EM field. This yields high-quality, rendering metasurfaces with toroidal dipoles effective for applications in sensing, filtering, and energy harvesting [16, 17]. The response of toroidal dipoles is usually very weak compared to electric and magnetic dipoles in natural materials. The toroidal dipoles can now become a dominant component in multipolar resonances with the advent of metasurfaces [18, 19]. The toroidal dipole excitation has been widely studied across microwave, terahertz, infrared, and visible frequency ranges [20-23]. However, most of the toroidal dipole based metasurfaces rely on either intentional symmetry breaking or carefully designed unit cells that are sensitive to the polarization state of the incident light [24]. These random polarization states limit the operational strength of the devices based on sensing and communication systems. Therefore, polarization-independent excitation of toroidal dipole in metasurfaces is a problem that is still under active research.

The characteristics of directional uniformity and polarization-independence are achieved by the structural symmetry in metasurfaces. The interaction between light and matter is very much influenced by such structural symmetries in optoelectronics [25, 26]. Progress has been made by leveraging high-symmetry unit cells such as circular resonators, symmetric patterns, and achiral metasurfaces that result in nearly identical transmission, reflection, and resonance characteristics for all polarization angles [27-29]. The most widely used approach for obtaining polarization independence is based on symmetric metasurfaces. Such symmetric structures exhibit polarization invariance due to their fourfold rotational symmetry, ensuring identical responses to all incident polarization states. However, these metasurface designs either suffer from low signal-to-noise ratios in sensing experiments, leading to issues for molecular differentiation, or are focused on obtaining large resonance modulations at the cost of quality factor [30, 31]. Achiral metasurfaces, characterized by their mirror symmetry and lack of handedness, demonstrate non-polarization selective behavior. This property is crucial for applications requiring an isotropic optical response [32]. The intrinsic symmetry in achiral metasurfaces enables polarization-independent wave propagation, a highly desired characteristic in integrated optical devices [33, 34]. They demonstrate consistent performance regardless of the angle of incidence and serve as the basis for both broadband and narrowband optical filters and reflectors in telecommunications.

Most of the studies on toroidal metasurfaces have been focused only on the passive tuning of the toroidal responses. The active tuning of the toroidal response increases its possibility of use where one requires several applications that provide a control over the response of the metasurface in a desirable manner [35]. In this context, recently active tuning of metasurface structures using phase-change materials (PCMs) has garnered a lot of attention. Recent developments in reconfigurable photonic devices have shown that phase-change materials can be used to design dynamically controlled optical systems [36-39]. $Ge_2Sb_2Te_5$ (GST) is a PCM characterized by two stable phases, each exhibiting unique optical and electrical properties [40]. GST is a widely studied PCM characterized by a significant contrast in properties between its amorphous (AGST) and crystalline (CGST) phases, along with rapid switching capabilities and minimal external power requirements [41-43]. Variations in GST properties enable parametric variation during operation in specific applications. However, only a limited work has been reported on the active tuning of toroidal resonance in GST metasurfaces.

Despite progress in both toroidal dipole metasurfaces and GST-enabled tunability, the integration of achiral polarization-independent toroidal dipole metasurfaces with active GST switching has not been comprehensively demonstrated in the mid-IR. In this work, the square spiral geometry is chosen for its intrinsic mirror symmetry, which eliminates handedness and supports electromagnetic response regardless of polarization state. The design is detailed through finite-difference time domain (FDTD) simulations and multipolar decomposition. Gold was selected as the plasmonic material due to its remarkable chemical inertness, demonstrating resistance to oxidation in humid or aqueous conditions [44]. The spiral structure embedded with GST on Au/SiO_2 platform supports toroidal excitation in the amorphous phase of GST whereas the resonance diminishes in the crystalline phase of GST, allowing real-time “switch-off” capability for the device.

2. Design and simulation methodology

Toroidal resonances in metasurfaces originate from a head-to-tail arrangement of magnetic dipoles generated by closed current loops, which can be realized using multiple spirals. Based on this concept, a square spiral structure with multiple branches was selected, as shown in Fig. 1. Its geometrical symmetry facilitates the equal distribution of currents and makes it polarization-independent. Fig. 1 illustrates the top and cross-sectional structure of the proposed spiral based metasurface design. The design mainly consists of two layers, with the upper layer composed of gold (Au) and containing embedded rectangular GST strips. The Au-GST embedded structure is supported by a SiO_2 insulator, the bottom layer, to facilitate the plasmon at the interface of both layers. The structure consists of multiple spiral branches separated by a uniform spacing s, where w denotes the width of each branch and d_{in} represents the inner dimension of the central square region. These parameters were optimized with respect to the resonance wavelength in the mid-infrared. Small gaps at the spiral ends allow to regulate the direction of the current, and prevent the traditional electric and magnetic dipole excitation and, in this way, increases the contribution of the toroidal dipole. The GST strips are arranged in a square spiral configuration comprising multiple variable loops to enhance toroidal dipole excitation. At a specific loop, the GST strips exhibit comparable dimensions on both sides and are evenly distributed from the center.

Electromagnetic confinement and plasmonic excitation conditions in the mid-infrared region define the thickness of the SiO_2 substrate and gold layer. A low-index SiO_2 layer supports efficient light trapping within the high-index metasurface by producing a significant refractive index contrast. Surface-bound modes like surface plasmon polaritons (SPPs) depend on sufficient optical isolation from the underlying environment, which is ensured by a thickness of 1 μm SiO_2 layer. This minimizes substrate leakage and suppresses radiation loss [45, 46]. The 200 nm thick layer of gold is chosen based on the optical skin depth of the gold in the mid-infrared. The thickness of the gold is much larger than its skin depth to ensure negligible transmission through the gold, and the induced currents on the surfaces are concentrated within the gold layer, which supports a strong plasmonic resonance. Simultaneously, this thickness permits adequate interaction of the evanescent fields in the metal-dielectric interface, which is necessary to generate localized surface plasmon resonance (LSPR) in the proposed metasurface [47, 48].

To further control the resonances, we incorporated the phase-change material GST into the spiral, which is placed on a SiO_2-Au base to minimize intrinsic losses. Since

AGST has a higher refractive index and insulator-like behavior, it must be and has been shown to be a good option for the escalation of various resonances caused by field confinement. This makes AGST a modulating element at the conductor-insulator interface of the SiO_2-Au interface. When the phase transitions to CGST, all resonances substantially decrease, making it more difficult to observe than AGST due to the lesser charge confinement. It is possible to turn the device on and off "in situ" by altering the spiral elements' material phase while other integrated components or "System-on-Chip" (SoC) type devices are operating.

The interaction of electromagnetic fields with the metasurface is assessed through a finite-difference time-domain (FDTD) solution utilizing Ansys Lumerical. Due to the repetitive nature of the structure, specific rules were applied in the *x* and *y* directions during simulations for a segment of the metasurface. A perfectly matched layer (PML) border consisting of 64 layers was implemented in the *z*-direction to eliminate unwanted reflections from the surroundings. The simulation region was divided into spatial grids measuring $dx = dy = dz = 1\ nm$, with the origin located at the center of the cell for precise field calculations. A plane-wave light source, characterized by an irradiation power of 3.3 μW and a bandwidth ranging from 0.5 μm to 2.5 μm, was directed perpendicularly to the metasurface in the negative *z*-direction. The distance from the source to the surface was 1 μm. The simulation time was established at 1 *ps*, corresponding to a pulse length of 10 *fs*. The experimental data from Palik [49] and Shportko *et al.* [50] were utilized to determine the complex refractive indices for SiO_2 and GST, respectively. PCM can transition between amorphous and crystalline states, facilitating tunability. Nevertheless, given that CGST and the gold layer exhibit comparable conductivity and dielectric properties, modifying the entire GST structure will effectively resemble modifying a singular thin layer. The couple's alternating branches have been activated to transition phases for the purpose of managing and monitoring the response shift.

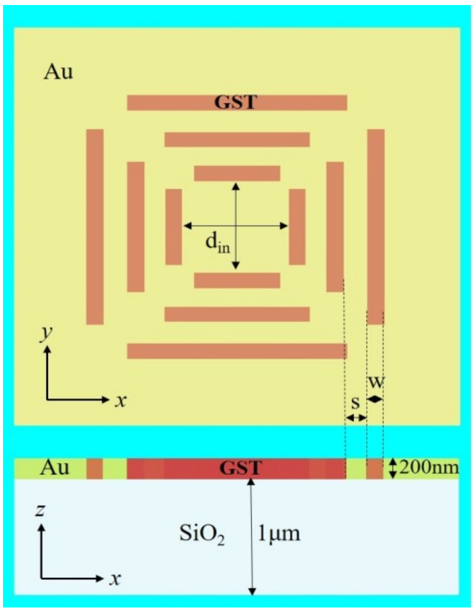

Fig. 1. Top and cross-sectional view of the proposed device having structural and parametric achirality (colour online)

Multipolar analysis has been utilized to illustrate the dominant resonances by decomposing the radiated power into contributions from various dipoles and quadrupoles. This process involves importing extracted parameters from FDTD and re-implementing them using the mathematical solver MENP, as detailed in the subsequent equations [51, 52]. The basic ingredient for any moment calculation *i.e.,* ‘volume current density, *j*’ can be calculated through frequency ω, permittivity of free space ε_0, refractive index *n* and electric field distribution *E(r)* (*r* is a position vector) in a designated contour as follows:

$$j = -i\omega\epsilon_o(n^2 - 1)E(r) \tag{1}$$

Followed by and using the above parameter along with dimension/contour, different moments can be calculated as follows:

Electric dipole moment:

$$P = \frac{1}{i\omega}\int jd^3r \tag{2}$$

Magnetic dipole moment:

$$M = \frac{1}{2C}\int (r\ x\ j)\ d^3r \tag{3}$$

Toroidal dipole moment:

$$T = \frac{1}{10C}\int [(r.j)r - 2r^2 j]d^3r \tag{4}$$

Electrical quadruple moment:

$$Q_{\alpha\beta} = \frac{1}{2i\omega}\int [r_\alpha j_\beta + r_\beta j_\alpha - \frac{2}{3}(r.j)\ \delta_{\alpha\beta}]\ d^3r \tag{5}$$

Magnetic quadruple moment:

$$M_{\alpha\beta} = \frac{1}{3C}\int [(rxj)_\alpha r_\beta + (rxj)_\beta r_\alpha]\ d^3r \tag{6}$$

Powers radiated by each moment (electric dipole moment I_p, magnetic dipole moment I_m, toroidal dipole I_T, electric quadruple moment I_{EQ}, and magnetic quadruple moment I_{MQ}) can be described as follows:

$$I_p = \frac{2\omega^4}{3C^3}\ |\ P\ |^2 \tag{7}$$

$$I_m = \frac{2\omega^4}{3C^3}\ |\ M\ |^2 \tag{8}$$

$$I_T = \frac{2\omega^6}{3C^5}\ |\ T\ |^2 \tag{9}$$

$$I_{EQ} = \frac{\omega^6}{5C^5}\sum |Q_{\alpha\beta}|^2 \tag{10}$$

$$I_{MQ} = \frac{\omega^6}{40C^5}\sum |M_{\alpha\beta}|^2 \tag{11}$$

where d^3r represents volume in integral, c is the speed of light in vacuum, $\delta_{\alpha\beta}$ is the delta function with (α, β) as coordinate system analogous to x, y, z.

3. Results and discussion

The proposed metasurface structure is analyzed for the inter-branch spacing *'s'* of 0.5 μm, 0.7 μm, and 1.0 μm. At each inter-branch spacing, the metasurface structure is simulated for rectangular GST branch widths of 0.1 μm, 0.2 μm, and 0.3 μm, respectively. The proposed structure is simulated for the wavelength range of 2 μm to 8 μm, which corresponds to the mid-infrared regime.

The electric field (E-field) distribution in Fig. 2(a) shows that electromagnetic energy is localized at the resonant wavelength of 3.7 μm. This confirms that a resonant mode has been excited in the metasurface structure. The high-intensity areas identified along the metallic segments correspond to localized charge accumulation and amplified electric dipole oscillations, confirming localized surface plasmon resonance (LSPR). These "hotspots" in the field show that electromagnetic energy is being effectively confined at the metal-dielectric contact. The low-field regions are, conversely, nodes of the standing wave pattern which exhibits less radiation loss and greater modal confinement. The vector field plot, as shown in Fig. 2(b), further illustrates circulating field patterns around the resonant regions. The above behaviour aligns with Maxwell's equations, wherein the spatial variation (curl) of the electric field induces magnetic field circulation, enabling continuous energy transfer within the structure. This relationship between the observation of strong localization of the electric field and closed-loop flow of the energy demonstrates the presence of a stable resonant mode, with efficient near-field confinement.

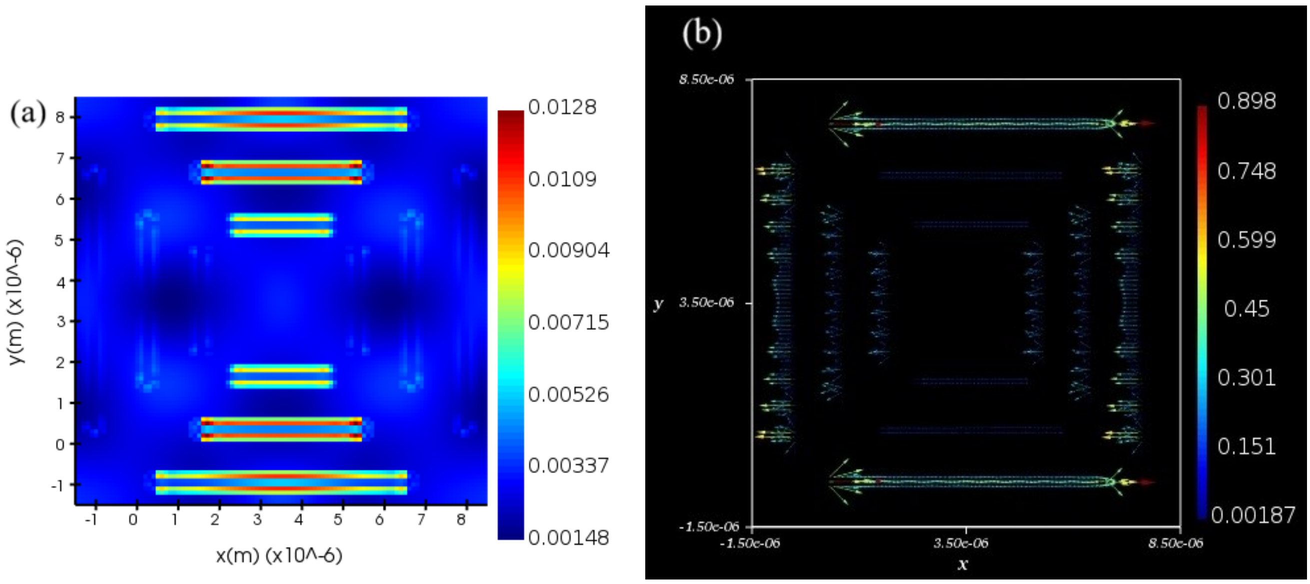

Fig. 2. (a) Electric field confinement (b) vector diagram showing the flow or direction of the field in AGST based structure at the surface of the device with branch width w =0.3 μm at 3.7 μm wavelength (colour online)

The transmission spectrum resonances of the three-turn spiral structure for inter-branch spacing of 0.5 μm, 0.7 μm, and 1 μm are shown in Figs. 3 (a), (b), and (c). Since the peaks remain intact at almost the same frequency locations for various dimensional alterations, it is clear that spacing has very little effect on the resonances. Therefore, it is clear that when spacing decreases, several peaks emerge for a given structure dimension. Higher-order collective mode production and mode-splitting explain this phenomenon. This could be explained by the fact that when two or more resonant elements are brought closer together, their unique resonances split into bonding and anti-bonding combinations. As a result, discrete sub-peaks may form as the gap between them shrinks, as shown clearly for spacing of 0.5 μm. Higher-order electromagnetic modes can be produced by further decreasing the gap, which enables current loops to flow over multiple turns at once. At neighboring frequencies, these appear as extra and weaker peaks clearly shown in Fig. 3(a). The inter-branch spacing of 0.7 μm offers an optimal trade-off between resonance strength, spectral clarity and electromagnetic coupling between spiral turns. This spacing, as demonstrated in the Fig. 3(b), produces sharp and profound transmission dip with all branch widths and does not produce over-broad resonance character that appears at smaller spacing, or weakened coupling that appears at larger spacing. In each of the three spacings, a systematic shift of the transmission with an increase in branch width w from 0.1 μm to 0.3 μm is observed, and resonance depth is greatly enhanced, as shown in Fig. 3(b). The wider the width, the stronger the displacement and conduction currents supported in the GST-Au hybrid layer, resulting in a higher field confinement.

The resonance effects become more pronounced as peak position, intensity, and full-width-half-maximum

(FWHM) vary with branch width. Peaks must be high and sharp (*i.e.,* have a reduced FWHM value) in addition to the desired operating frequency in order to meet the requirements of any resonance. In Fig. 3(d), the previously indicated characteristics have been further shown in relation to the spiral branches' changing width. The sharpness is diminishing as width increases because it is evident that the FWHM and peak frequency are rising with width. Additionally, as width grows, resonance intensity decreases. One can notice trade-offs in various parameters. However, a number of congruity effects explain these occurrences collectively, creating an analogy of a spiral structure that exhibits intrinsic losses, capacitance, and inductance (both mutual and self). A blue shift in resonance can be seen as a result of increasing branch width because it changes the distribution of surface currents, which can upset the delicate balance needed for strong toroidal dipole recitation as inductance drops. Due to the increased electric dipole contribution, wider branches may increase ohmic and radiation losses, resulting in a faster energy dissipation and a lower FWHM (quality factor). The coupling between neighboring resonators can be impacted by changes in width, which can change the collective behavior required for acute resonances. Peak amplitudes drop as a result of field confinements because the volume of modes reduces with increasing surface area/coupling area.

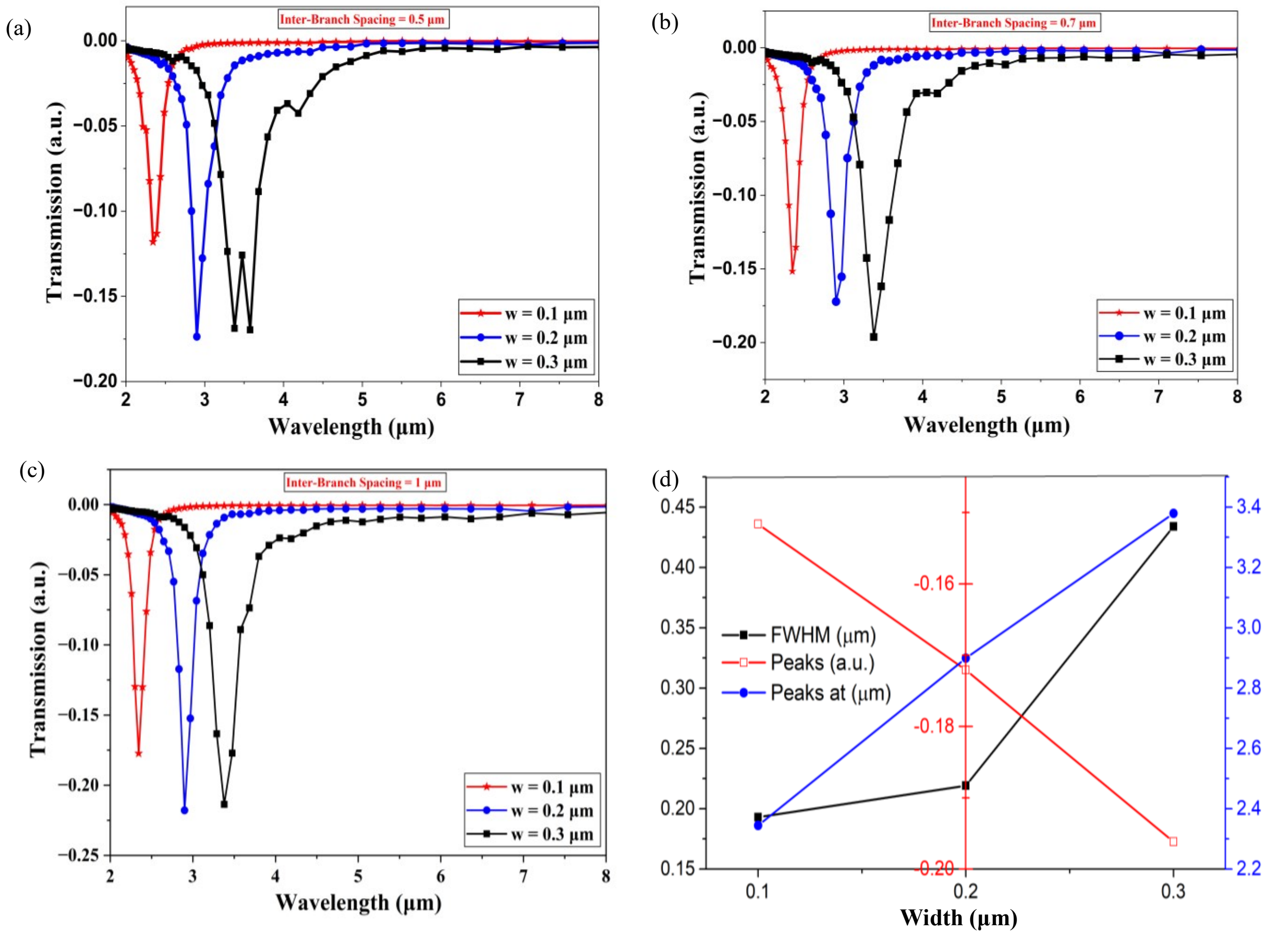

Fig. 3. Transmission spectrum of resonances of the structure having different branch width w with different inter-branch spacing of (a) s = 0.5 μm (b) s = 0.7 μm and (c) s = 1 μm. (d) variation and comparison of FWHM, peak response, and peak frequency with respect to change in branch width w (colour online)

Additionally, it is necessary to identify the type of resonance that predominates in the system among the several phenomena observed in such similar or other devices before proceeding with the parametric analysis of resonance. In order to verify this, vector diagrams of surface current *j (A/m)* displaying magnitude and direction at various *xy*-plane coordinates have been retrieved from the surface for various dimensions and related resonance frequencies, as illustrated in Fig. 4. With the aid of charge direction/revolution, which is shown in each panel, distinct evidence of toroidal dipole resonance can be seen. For a branch width of 0.3 *μm* and a wavelength of approximately 3.7 *μm*, Fig. 4(a), (b), and (c) were collected with 0.5 *μm*, 0.7 *μm*, and 1 *μm* spacing between branches. The turbulence intensity may grow with increasing separation, which makes sense because there is more room for charge movements. On the other hand, their coupling strength may decrease, as evidenced by the enlarged poles on the surface.

This has an impact on the resonance's FWHM and overall intensity. There may be a few additional resonances in addition to toroidal ones, as well as the quadrupoles seen in Fig. 4(d). In these situations, we have performed multipolar analysis using current density, which is covered in the section that follows. The introduction section has already covered the multipolar equations and implementation.

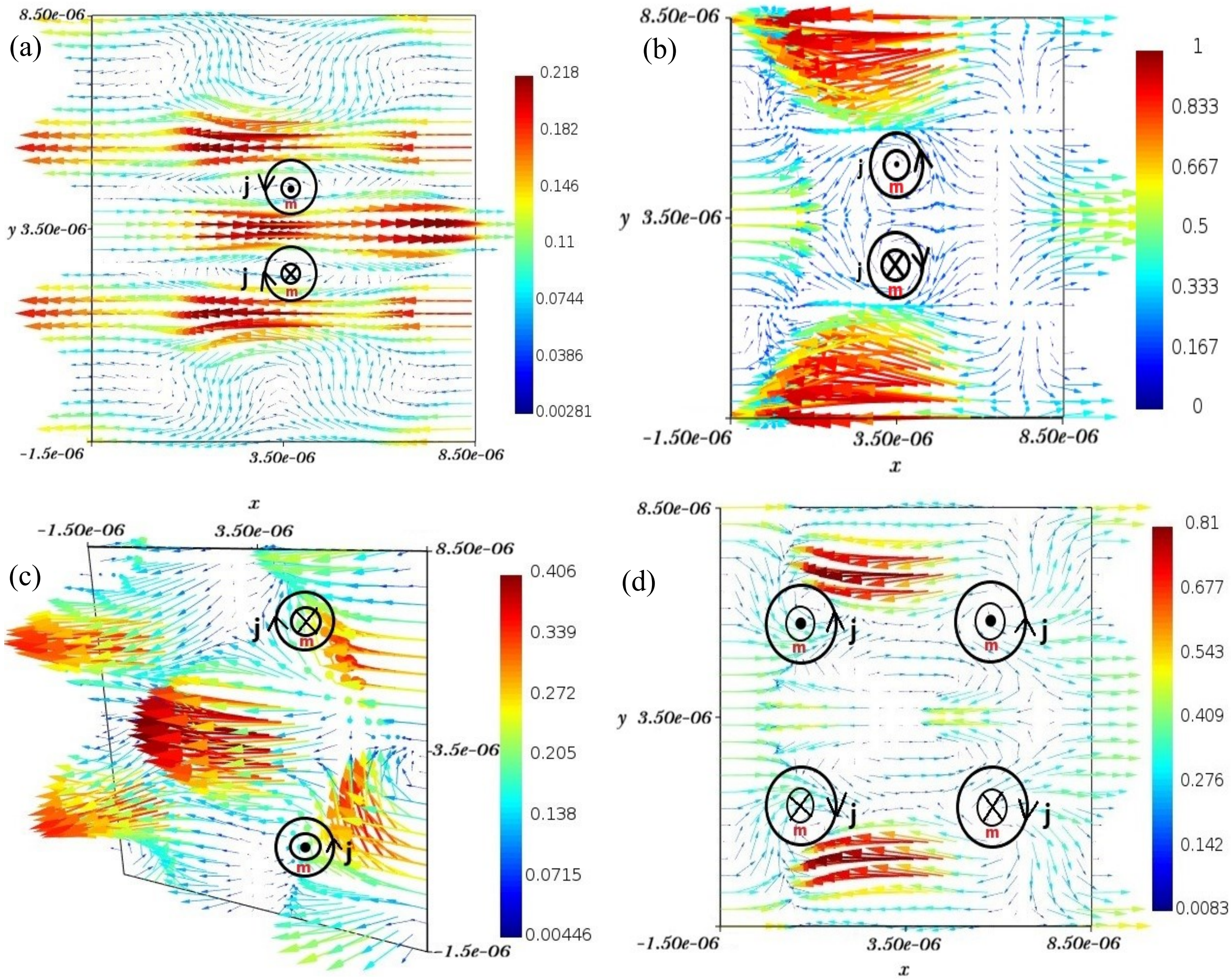

Fig. 4. Current density j vector plot showing the formation of dipoles in antiparallel directions hence making toroidal dipole T for device having branch with w = 0.3 μm at wavelength of 3.7 μm for spacing between turns (a) s = 0.5 μm (b) s = 0.7 μm and (c) s = 1 μm. (d) Quadrupoles also has been observed at a few instances (colour online)

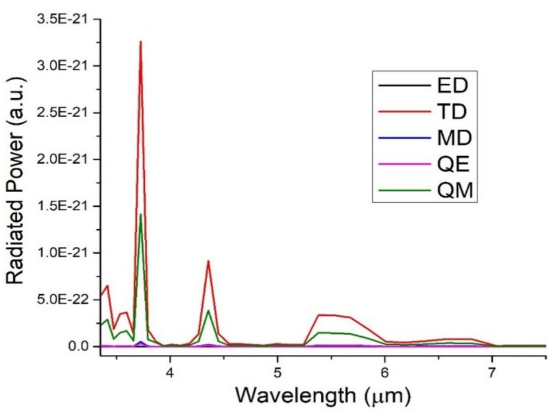

Fig. 5. Multipolar plot in terms of radiated power for electric dipole (ED), magnetic dipole (MD), toroidal dipole (TD), electric quadruple (QE) and magnetic quadruple (QM) (colour online)

It is evident from Fig. 5's multipolar plots of the suggested device's radiated power that the toroidal resonance predominates over other, weaker resonances. Around 3.7 μm is the highest toroidal dipole, with weaker peaks at a few other wavelengths. In addition to this toroidal magnetic quadrupole, the second dominant resonance type appears to be following the toroidal resonance since it occurs at precisely the same wavelengths and frequencies. This could be because of the type of symmetric structure that produces double dipoles, as seen in the Figs. 2(b) and 4(d), where the parallel sides of the incident light EM field direction accommodate the maximum field strength. For the same dimensional analysis, a very small portion can also be seen induced on the perpendicular sides.

As can be seen from the structure's symmetry, the structure is dubbed achiral since the study was expanded to include the change in the EM field's direction without affecting any spectrum or results. Moreover, it has slight effects on the incident light's angle, which can reveal the suggested device's angle/polarity independence. This makes it appropriate for a non-invasive mid-infrared sensor in a variety of application domains, regardless of its actual location and orientation.

4. Conclusion

This research introduces a novel achiral metasurface structure engineered to realize switchable toroidal dipole resonances in the mid-infrared regime using phase-change material GST. Through rigorous FDTD simulation and multipolar analysis, the study demonstrates that the square spiral architecture embedded with GST on a SiO_2/Au platform effectively supports field confinement and toroidal excitation when GST is in the amorphous phase (AGST). When transformed to the crystalline phase (CGST), the resonant features diminish drastically, allowing real-time "switch-off" capability for the device- an innovative approach for tunable mid-infrared photonic components. The investigation reveals that while spacing between spiral turns has a subtle effect on the resonance frequencies, it significantly impacts the emergence of multiple peaks due to mode splitting and collective higher-order interactions. More critically, the branch width strongly affects resonance intensity, peak location, and full-width half-maximum (FWHM), thus influencing the quality factor and sensitivity of the resonant behavior. A clear trade-off is established between structural dimensions and spectral performance, enabling design optimization for specific applications. The device's robustness against polarization changes and angular incidence further enhances its applicability in complex and dynamic environments, such as bio-sensing, stealth technology, and non-invasive diagnostic tools. Additionally, the multipolar analysis confirms that toroidal dipoles remain the dominant mode under optimized structural configurations, offering a high Q-factor essential for next-generation optical sensing platforms. In summary, this work advances the frontier of metasurface engineering by demonstrating a polarization-independent, dynamically reconfigurable photonic platform, laying a strong foundation for future system-on-chip photonic architectures and mid-infrared regime functional devices.

References

[1] J. C. Zhang, G. B. Wu, M. K. Chen, X. Che, Y. Liang, D. P. Tsai, C. H. Chan, Electromagnetic Science **1**, 0030131 (2023).

[2] S. D. Assimonis, S. Chandravanshi, O. Yurduseven, D. Zelenchuk, O. Malyuskin, M. A. B. Abbasi, V. Fusco, S. L. Cotton, Sensors **21**, 8452 (2021).

[3] A. Valipour, M. H. Kargozarfard, M. Rakhshi, A. Yaghootian, H. M. Sedighi, Proceeding of the Institution of Mechanical Engineers, Part L: Journal of Materials: Design and Applications **236**, 2171 (2021).

[4] F. Marvi, K. Jafari, Nanotechnology **33**, 265502 (2022).

[5] J. Zhang, N. Mu, L. Liu, J. Xie, H. Feng, J. Yao, T. Chen, W. Zhu, Biosens. Bioelectron. **185**, 113241 (2021).

[6] H. Zhou, C. Zhang, Light-Sci. Appl. **12**, 287 (2023).

[7] A. Bansal, C. Panagamuwa, W. Whittow, IEEE Antennas and Propagation Magazine **66**, 40 (2024).

[8] M. S. Khan, R. A. Shakoor, O. Fayyaz, E. M. Ahmed, Optik **297**, 171575 (2024).

[9] Y. Li, F. Liu, M. Zheng, Y. Tang, J. Han, The European Physical Journal D **78**, 148 (2024).

[10] H. M. Zamel, S. I. Abd El-Rahman, A. M. Attiya, Scientific Reports **14**, 21316 (2024).

[11] S. Anwar, Transactions on Electrical and Electronic Materials **25**, 722 (2024).

[12] M. A. Butt, M. Juchniewicz, M. Słowikowski, Ł. Kozłowski, R. Piramidowicz, Sensors **25**, 1102 (2025).

[13] Q. Li, S. Yu, Z. Li, W. Liu, H. Cheng, S. Chen, Nanophotonics **14**, 1045 (2025).

[14] M. F. Limonov, M. V. Rybin, A. N. Poddubny, Y. S. Kivshar, Nat. Photonics **11**, 543 (2017).

[15] M. Gupta, R. Singh, Adv. Opt. Mater. **4**, 2119 (2016).

[16] V. R. Tuz, V. V. Khardikov, Y. S. Kivshar, ACS Photonics **5**, 1871 (2018).

[17] B. Luk'yanchuk, N. I. Zheludev, S. A. Maier, N. J. Halas, P. Nordlander, H. Giessen, C. T. Chong, Nat. Mater. **9**, 707 (2010).

[18] H. Zhong, L. Huang, S. Li, C. Zhou, S. You, L. Li, Y. Cheng, A. E. Miroshnichenko, Appl. Phys. Rev. **11**, 031404 (2024).

[19] R. Jin, L. Huang, C. Zhou, Z. Fu, J. Chen, J. Wang, X. Li, F. Yu, J. Chen, Nano Letters **23**, 9105 (2023).

[20] Y. Wang, Z. Han, Y. Du, J. Qin, Nanophotonics **10**, 1295 (2021).

[21] M. Kang, T. Liu, C. Chan, M. Xiao, Nat. Rev. Phys. **5**, 659 (2023).

[22] T. Sang, Q. Mi, C. Yang, X. Zhang, Y. Wang, Y. Ren, T. Xu, Nanophotonics **13**, 1369 (2024).

[23] M. Qin, G. Wei, H. Xu, R. Ma, H. Li, W. Gao, J. Liu, F. Wu, Appl. Phys. Lett. **124**, 051703 (2024).

[24] W. Wang, J. Qi, Applied Physics Express **12**, 065004 (2019).

[25] D. L. Andrews, Symmetry **13**, 1368 (2021).

[26] Y. Li, J. Ling, J. Guo, Q. Li, D. Zhong, X. Wang, Photonics **11**, 824 (2024).

[27] P. Vaity, H. Gupta, A. Kala, S. D. Gupta, Y. S. Kivshar, V. R. Tuz, V. G. Achanta, Advanced Photonics Research **3**, 2100144 (2022).

[28] X. Wang, S. Li, C. Zhou, Opt. Express **28**, 11983 (2020).

[29] R. M. Saadabad, L. Huang, A. E. Miroshnichenko, Phys. Rev. B **104**, 235405 (2021).

[30] H. Zhong, T. He, Y. Wang, T. Qi, Y. Meng, D. Li, P. Yan, Q. Xiao, Opt. Express **32**, 5862 (2024).

[31] Y. Cai, Y. Huang, K. Zhu, H. Wu, Opt. Lett. **46**, 4049 (2021).
[32] X. Wan, Y. Li, Y. Wang, Yifan Li, C. Zhang, Symmetry **17**, 1001 (2025).
[33] M. Khorasaninejad, A. Y. Zhu, C. Roques-Carmes, W. T. Chen, J. Oh, I. Mishra, R. C. Delvin, F. Capasso, Nano Letters **16**, 7229 (2016).
[34] T. Sun, J. Hu, S. Ma, F. Xu, C. Wang, Opt. Express **29**, 31902 (2021).
[35] G. Liu, X. Zhai, S. Xia, Q. Lin, C. Zhao, L. Wang, Opt. Express **25**, 26045 (2017).
[36] H. Ren, J. Pang, N. Jia, R. Chen, S. Gao, T. Cao, ACS Applied Optical Materials **3**, 2673 (2025).
[37] J. Pang, H. Ren, R. Chen, Y. Ren, Y. Wu, Q. Yi, L. Shen, S. Zhang, T. Cao, Laser & Photonics Review **19**, e00281 (2025).
[38] S. Gao, T. Cao, H. Ren, J. Pang, R. Chen, Y. Ren, Z. Zhao, X. Chen, D. Guo, Opto-Electronic Technology **1**, 250002 (2025).
[39] S. Tripathi, R. K. Mishra, Optik **307**, 171827 (2024).
[40] W. Tao, Y. Wu, F. Zhao, C. Li, B. Fang, X. Jing, M. Yu, Optics & Laser Technology **177**, 111064 (2024).
[41] G. B. Beneventi, L. Perniola, Q. Hubert, A. Gliere, I. Larcher, P. Pavan, B. D. Salvo, IEEE Transactions on Electron Devices **59**, 188 (2012).
[42] H. S. P. Wong, S. Raoux, S. Kim, J. Liang, J. P. Reifenberg, B. Rajendran, M. Asheghi, K. E. Goodson, Proceedings of IEEE **98**, 2201 (2010).
[43] S. Tripathi, V. Srivastava, Sunny, R. K. Mishra, Indian Journal of Physics **97**, 3637 (2023).
[44] Z. Guo, Z. Fan, X. Kong, Z. Meng, Opt. Commun. **461**, 125233 (2020).
[45] S. A. Maier, Plasmonics: Fundamentals and Applications, Springer, 2007.
[46] H. Raether, Surface Plasmons on Smooth and Rough Surfaces and on Gratings, Springer, 1988.
[47] P. B. Johnson, R. W. Christy, Phys. Rev. B **6**, 4370 (1972).
[48] N. Yu, F. Capasso, Nat. Mater. **13**, 139 (2014).
[49] E. D. Palik, Handbook of Optical Constants of Solids, Academic Press, 1985.
[50] K. Shportko, S. Kremers, M. Woda, D. Lencer, J. Robertson, M. Wuttig, Nat. Mater. 7, 653 (2008).
[51] H. S. Ee, R. Agarwal, Nano Lett. 16, 2818 (2016).
[52] P. Mishra, V. Srivastava, M. Kumar, Sunny, Journal of Electronic Materials 50, 6748 (2021).

*Corresponding author: shirisht.phd20.ec@nitp.ac.in